A CS-Enhanced Approach for Near-Field Antenna Characterization Subject to Truncation Error

M. Salucci, N. Anselmi, and A. Massa

2024/04/26

Contents

1 Plane dimension side : $\zeta_{meas} = 8\,[\lambda]$

Original (*OMP*) MbD parameters

- Max. number of iterations of the OMP algorithm : $I = \{1; 2; 3; ...; 20\}$;
- Selected iteration to report the results: $I = 3$; this choice is justified by the fact that at this iteration the *OMP* algorithm reaches the best near field error as shown in the following Fig. 1.

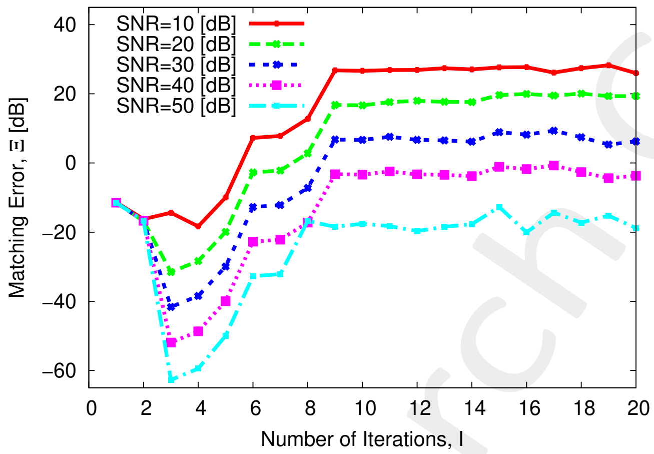

Figure 1: Behaviour of the near-field matching error versus the number of *OMP* iterations, I.

Evaluation of the Truncation Error from Actual Near-Field Data

In order to evaluate the truncation error, in the following figure is predented a visual comparison of the near-field radiated by the *AUT* measured over the full interpolation plane (ζ_{int}) and on the truncated region (ζ_{meas}), as well as the corresponding far-field patterns obtained with NF-FF transformation. The truncated near-field has been obtained as follows:

$$E_{tr}(x,y) = \begin{cases} E(x,y) \quad if & -\frac{\zeta_{meas}}{2} \leq \tau \leq \frac{\zeta_{meas}}{2} \\ 0 & otherwise \end{cases} \quad ; -\frac{\zeta_{int}}{2} \leq \tau \leq \frac{\zeta_{int}}{2}$$

where $\tau = x,\ y$.

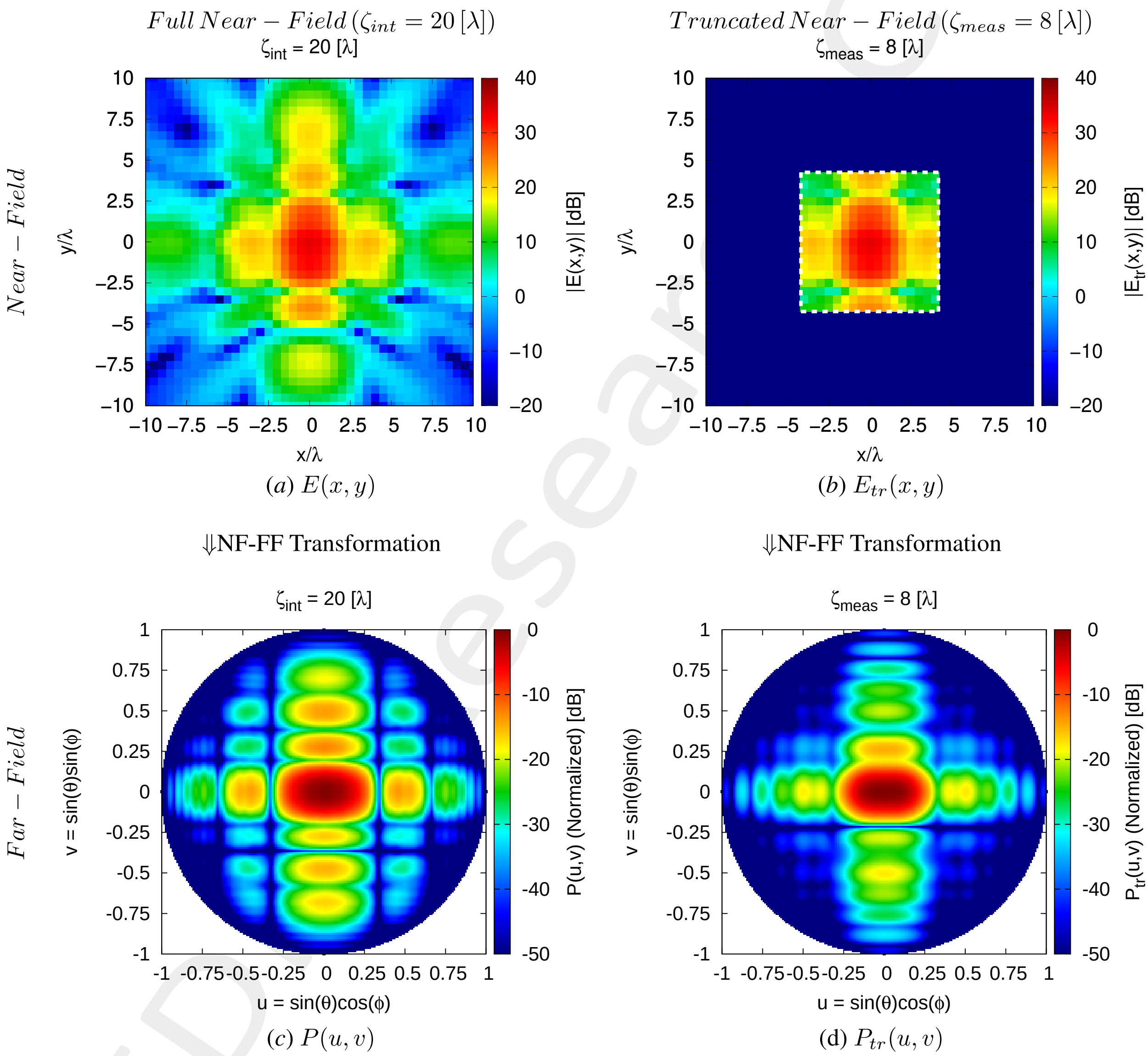

Figure 2: $\zeta_{meas} = 8\,[\lambda]$ - $(a)(b)$ Near-field and $(c)(d)$ far-field patterns obtained via NF-FF transformation for the actual *AUT*.

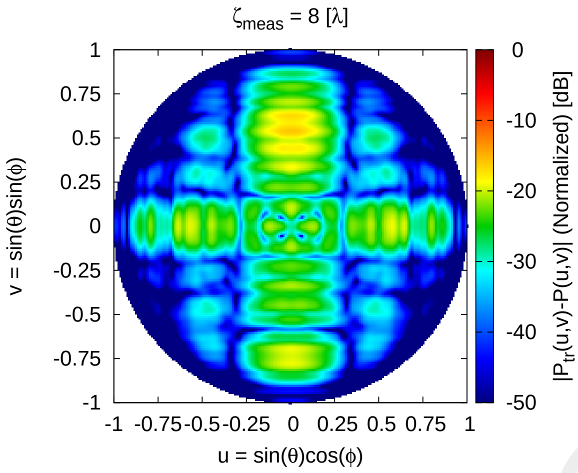

Figure 3: $\zeta_{meas} = 8\,[\lambda]$ - Difference between the full and the truncated far-fields, $|P(u,v) - P_{tr}(u,v)|$.

Near-Field Error

The comparison, in terms of near field error, between the original (*OMP*) and the alternative (*BCS*) MbD is reported in the following Fig. 4:

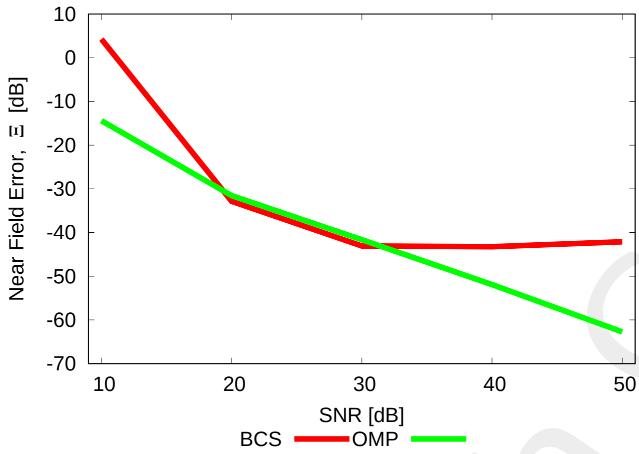

Figure 4: Near Field Error comparison between original (*OMP*) and alternative (*BCS*) MbD for different SNR values

$SNR\,[dB]$	*Near Field Error,* Ξ $[dB]$	
	BCS	OMP
50	-42.12	-62.73
40	-43.25	-51.92
30	-43.09	-41.64
20	-32.85	-31.55
10	4.26	-14.39

Table I: Near Field Errors obtained by the original (*OMP*) and alternative (*BCS*) MbD

Observations

The *OMP* and *BCS* solvers performance are not good for $10 \leq SNR \leq 20\,[dB]$ because the near-field error is $\Xi > -20\,[dB]$. For $SNR > 20\,[dB]$:

- the *OMP* error decreases linearly with the increase of the SNR value obtaining the best performance;
- the *BCS* obtains results comparable to that of the *OMP* in the range $20\,[dB] \leq SNR \leq 30\,[dB]$, but then its error remains almost constant while the *OMP* error decreases.

Estimated Near-Field

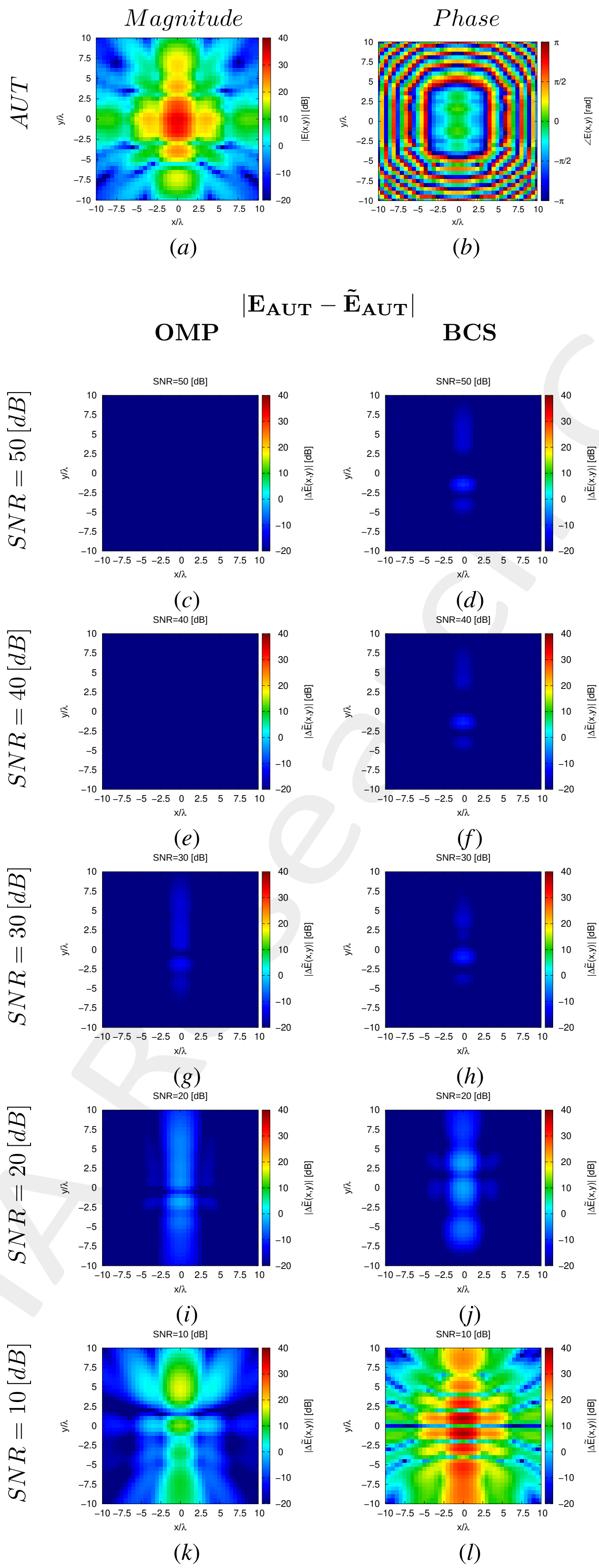

Figure 5: Magnitude difference between the actual and estimated $2-D$ near-field pattern when processing noisy measurements at different SNRs.

Estimated Far-Field

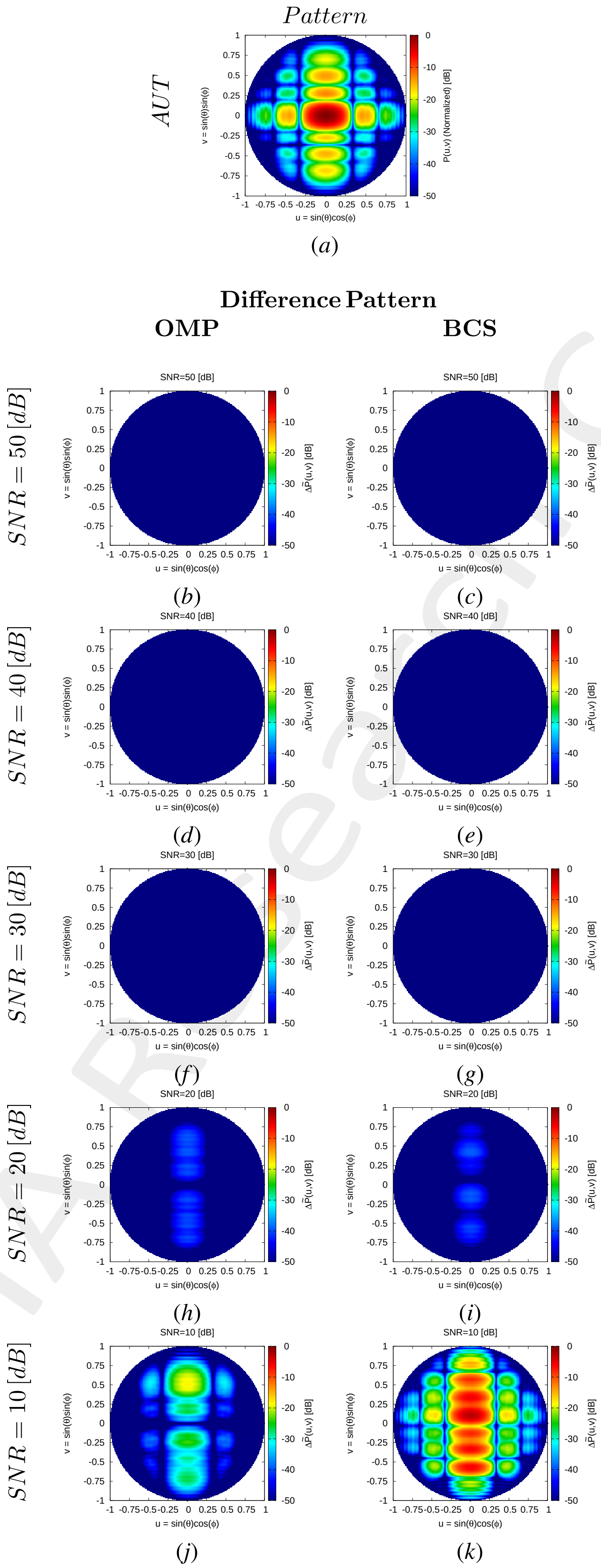

Figure 6: Difference between the actual and estimated $2-D$ far-field pattern when processing noisy measurements at different SNRs.

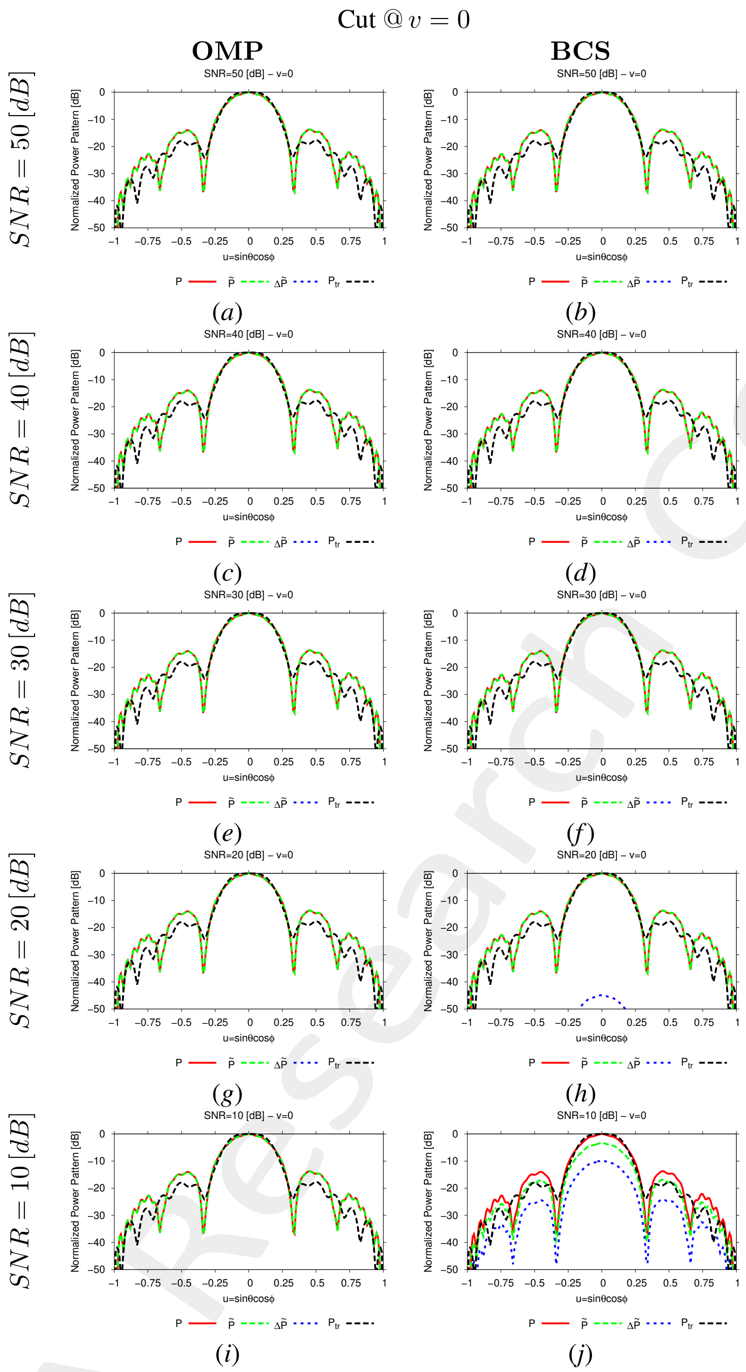

Figure 7: $1-D$ cuts of the estimated far-field pattern (obtained through near-to-far-field transformation from the estimated near-field patterns) under several noisy conditions

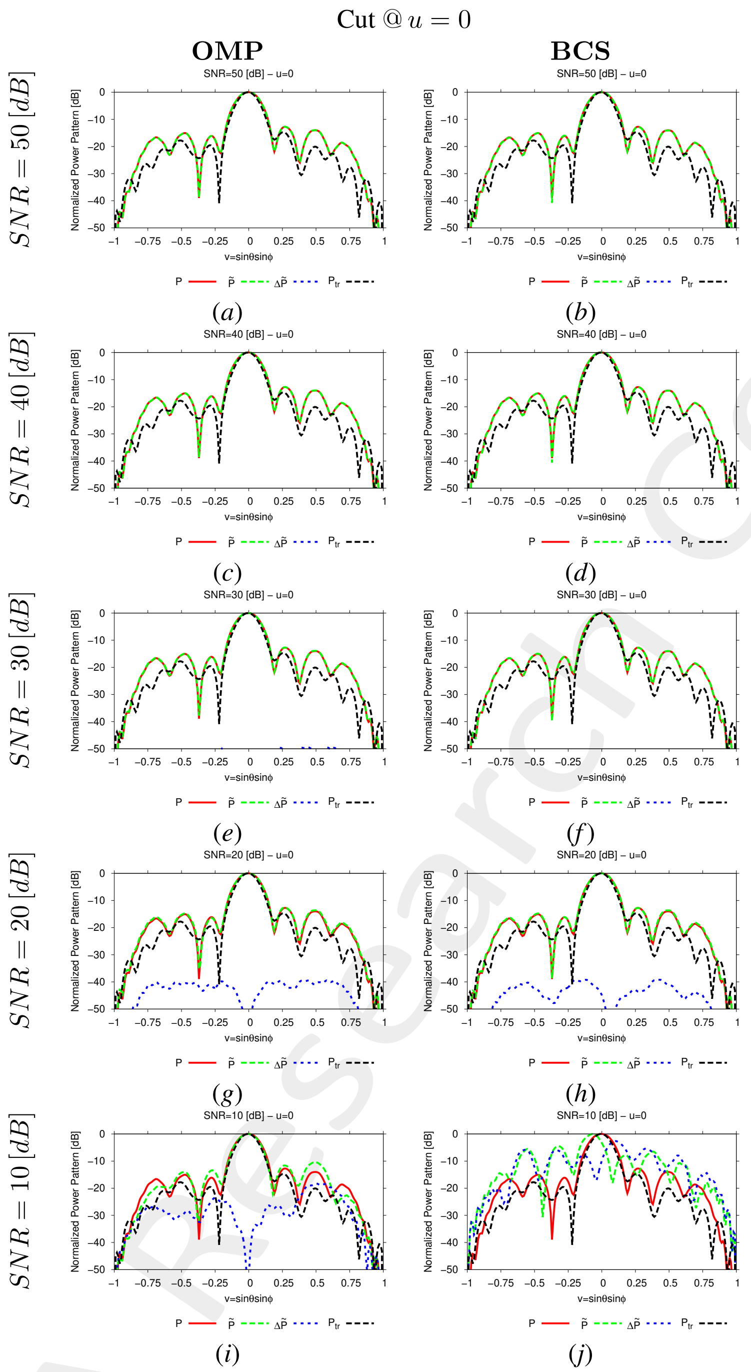

Figure 8: $1-D$ cuts of the estimated far-field pattern (obtained through near-to-far-field transformation from the estimated near-field patterns) under several noisy conditions

$SNR\,[dB]$	$Far-Field\ Error,\ \chi\ [dB]$	
	BCS	OMP
50	−43.64	−63.72
40	−44.97	−52.80
30	−44.54	−42.52
20	−33.61	−32.42
10	0.36	−15.64

Table II: Far-field matching error between the actual and estimated AUT patterns (both obtained through near-to-far-field transformation from the corresponding near-field patterns) under several noisy conditions.

Estimated Coefficients

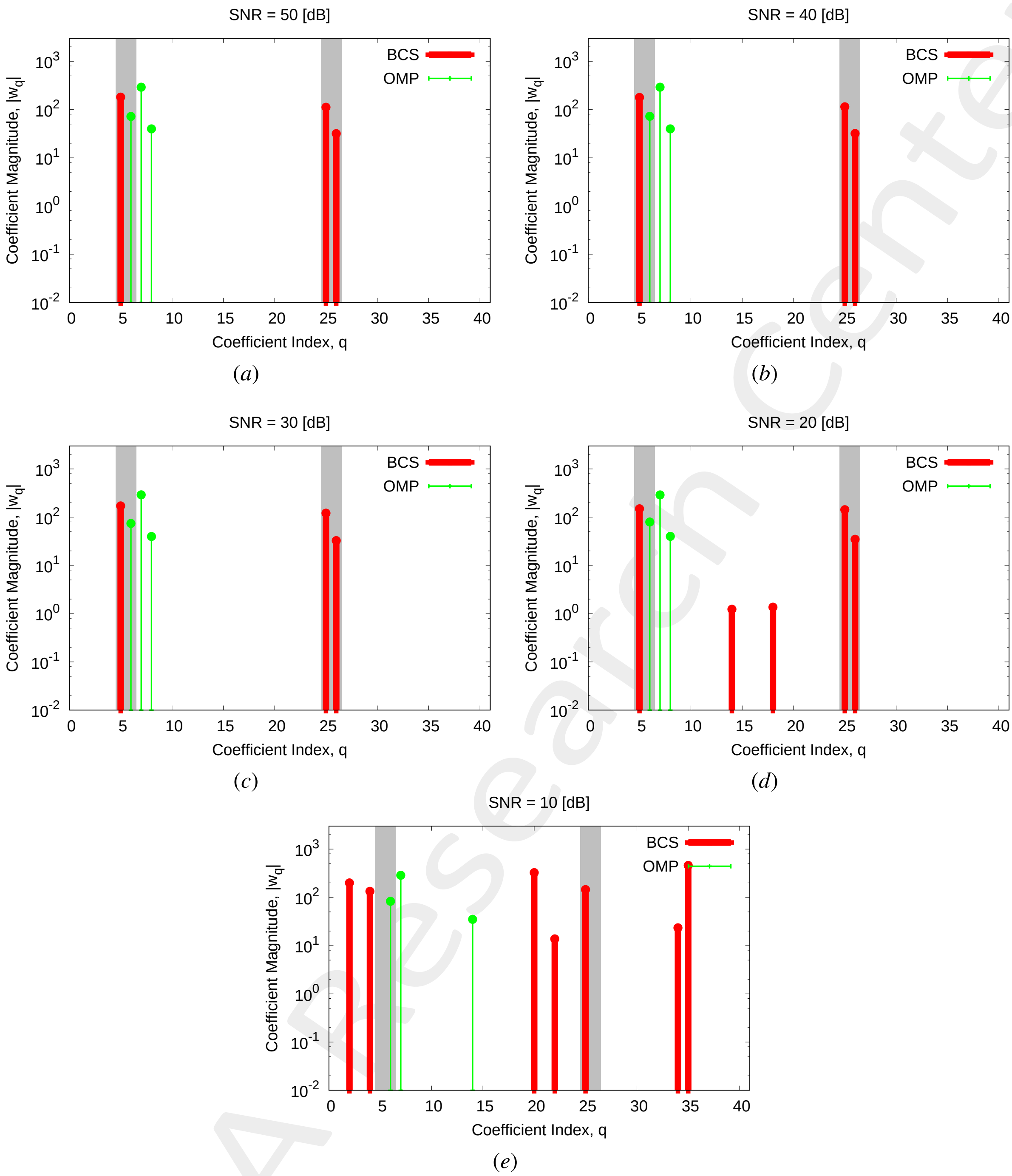

Figure 9: Coefficient comparison between original (*OMP*) and alternative (*BCS*) MbD : (*a*) $SNR = 50\,[dB]$, (*b*) $SNR = 40\,[dB]$, (*c*) $SNR = 30\,[dB]$, (*d*) $SNR = 20\,[dB]$, (*e*) $SNR = 10\,[dB]$

Observations

The considered *AUT* is characterized by a magnitude failure of an antenna element and a phase failure of another antenna element (i.e., $\nu^{(3)} = 0.45$ and $\gamma^{(3)} = \frac{\pi}{3}\,[rad]$):

- the *OMP* selects vectors related only to magnitude failures and whatever the SNR this algorithm detects the magnitude failure even if the detection is not precise since other vectors not connected to the current failures are chosen. The *OMP* fails in detecting the phase failure affecting the *AUT* because none of the vectors related to the actual phase failure has been selected.

- the *BCS* algorithm is able to identify both the failures affecting the AUT even if the failure detections are not precise particularly for low SNR values since the method selects also vectors not connected to the actual failures and it doesn't pick all the vectors of the failures affecting the *AUT*.

Computational times

- Δt_{Sim}: Time required to simulate the K *AUT* configurations used to build the $(T \times K)$ "pattern matrix";
- Δt_{SVD}: Time required to perform the *SVD* of the $(T \times K)$ "pattern matrix";
- $\Delta t_{MbE}^{OMP/BCS}$: (Mean) Time required by the Measurement-by-Example tool to read the *SVD* output and perform the estimation of the *AUT* radiated field.

Δt_{Sim} $[sec]$	4.17×10^4
Δt_{SVD} $[sec]$	1.53×10^2
Δt_{MbE}^{BCS} $[sec]$	1.43×10^{-1}
Δt_{MbE}^{OMP} $[sec]$	8.30×10^{-2}

Table III: Computational times

Remarks

- Given that the number of simulated *AUT*s is $K = S \times (F^{(s)} + P^{(s)}) = 120$, the average per-*AUT* simulation time is

$$\Delta t_{FEKO} \simeq \frac{\Delta t_{Sim}}{K} = \frac{4.17 \times 10^4}{120} [sec] = 3.47 \times 10^2 \, [sec]$$

1.0.1 Plane dimension side : $\zeta_{meas} = 4\,[\lambda]$

Original (*OMP*) MbD parameters

- Max. number of iterations of the OMP algorithm : $I = \{1;\, 2;\, 3;\, ...;\, 20\}$;
- Selected iteration to report the results: $I = 1$; this choice is justified by the fact that at this iteration the *OMP* algorithm reaches the best near field error as shown in the following Fig. 10.

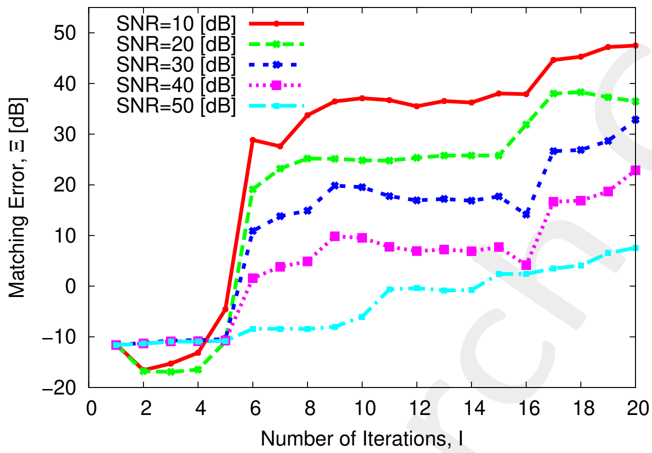

Figure 10: Behaviour of the near-field matching error versus the number of *OMP* iterations, I.

Evaluation of the Truncation Error from Actual Near-Field Data

In order to evaluate the truncation error, in the following figure is predented a visual comparison of the near-field radiated by the *AUT* measured over the full interpolation plane (ζ_{int}) and on the truncated region (ζ_{meas}), as well as the corresponding far-field patterns obtained with NF-FF transformation. The truncated near-field has been obtained as follows:

$$E_{tr}(x,y) = \begin{cases} E(x,y) & if \quad -\frac{\zeta_{meas}}{2} \leq \tau \leq \frac{\zeta_{meas}}{2} \\ 0 & otherwise \end{cases} \quad ; -\frac{\zeta_{int}}{2} \leq \tau \leq \frac{\zeta_{int}}{2}$$

where $\tau = x,\, y$.

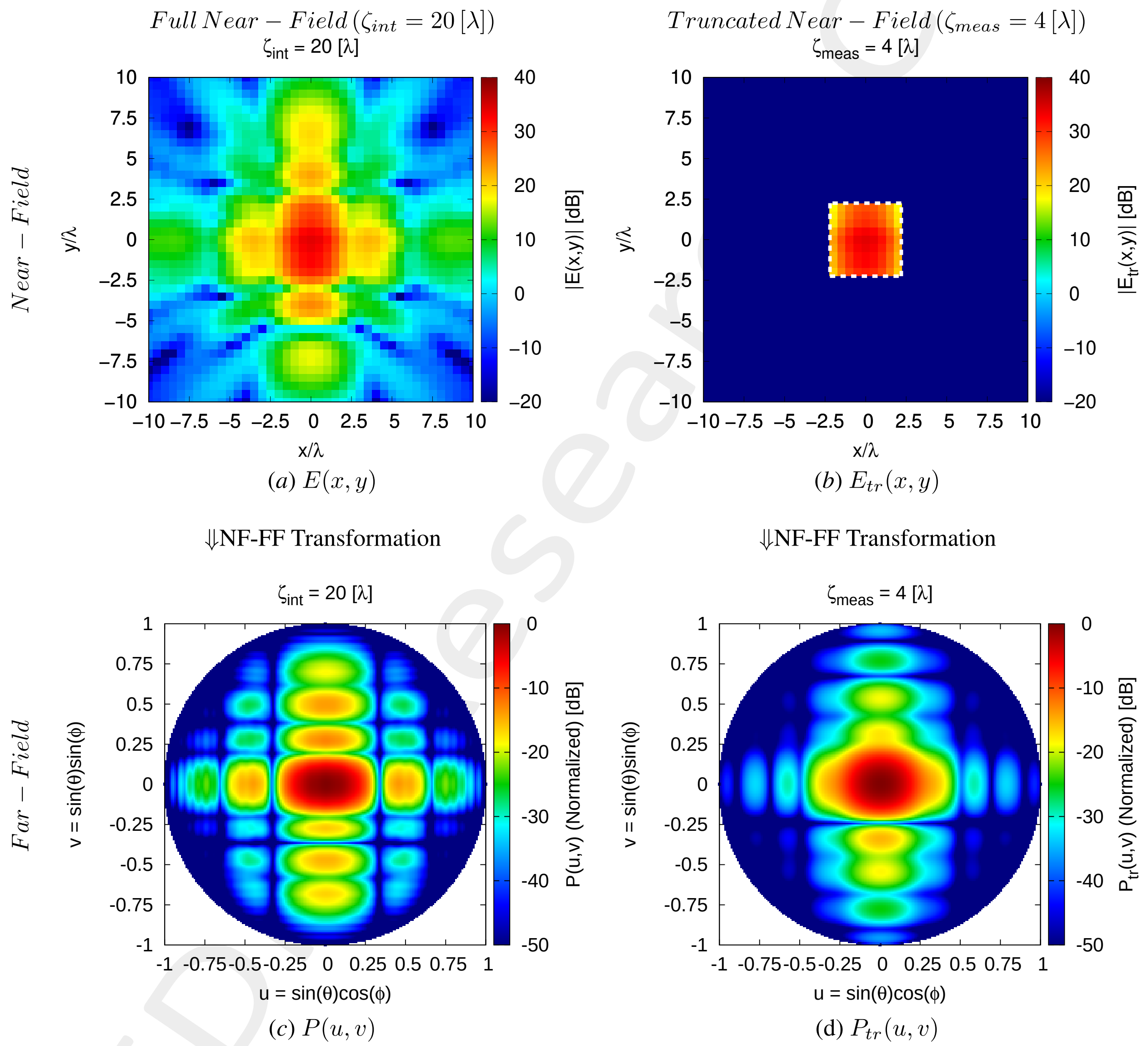

Figure 11: $\zeta_{meas} = 4\,[\lambda]$ - $(a)(b)$ Near-field and $(c)(d)$ far-field patterns obtained via NF-FF transformation for the actual *AUT*.

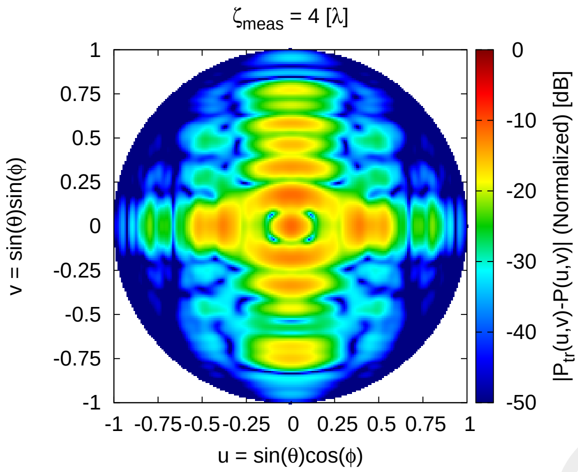

Figure 12: $\zeta_{meas} = 4\,[\lambda]$ - Difference between the full and the truncated far-fields, $|P(u,v) - P_{tr}(u,v)|$.

Near-Field Error

The comparison, in terms of near field error, between the original (*OMP*) and the alternative (*BCS*) MbD is reported in the following Fig. 13:

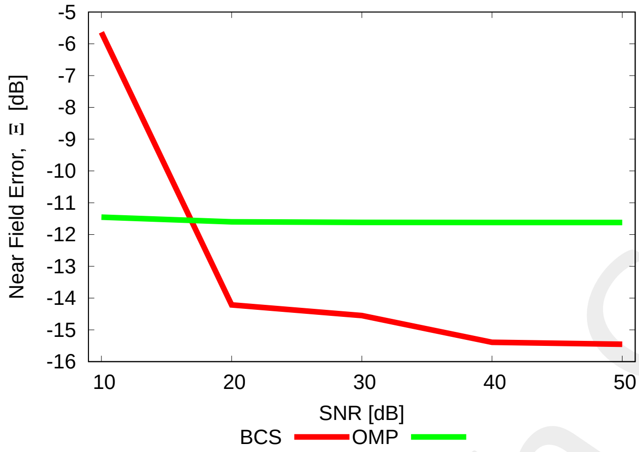

Figure 13: Near Field Error comparison between original (*OMP*) and alternative (*BCS*) MbD for different SNR values

$SNR\,[dB]$	*Near Field Error,* Ξ $[dB]$	
	BCS	OMP
50	-15.45	-11.62
40	-15.39	-11.62
30	-14.55	-11.62
20	-14.22	-11.60
10	-5.64	-11.45

Table IV: Near Field Errors obtained by the original (*OMP*) and alternative (*BCS*) MbD

Observations

By observing the results reported in Fig. 13 it is possible to point out that both the employed algorithms perform poorly with the considered measurement set-up. In particular:

- the *OMP* error remains almost constant at an error value $\Xi \sim -11\,[dB]$ which does not permit a good near-field reconstruction;
- the *BCS* results are slightly better than those of the *OMP* solver but not enough to allow an accurate near-field reconstruction.

Estimated Near-Field

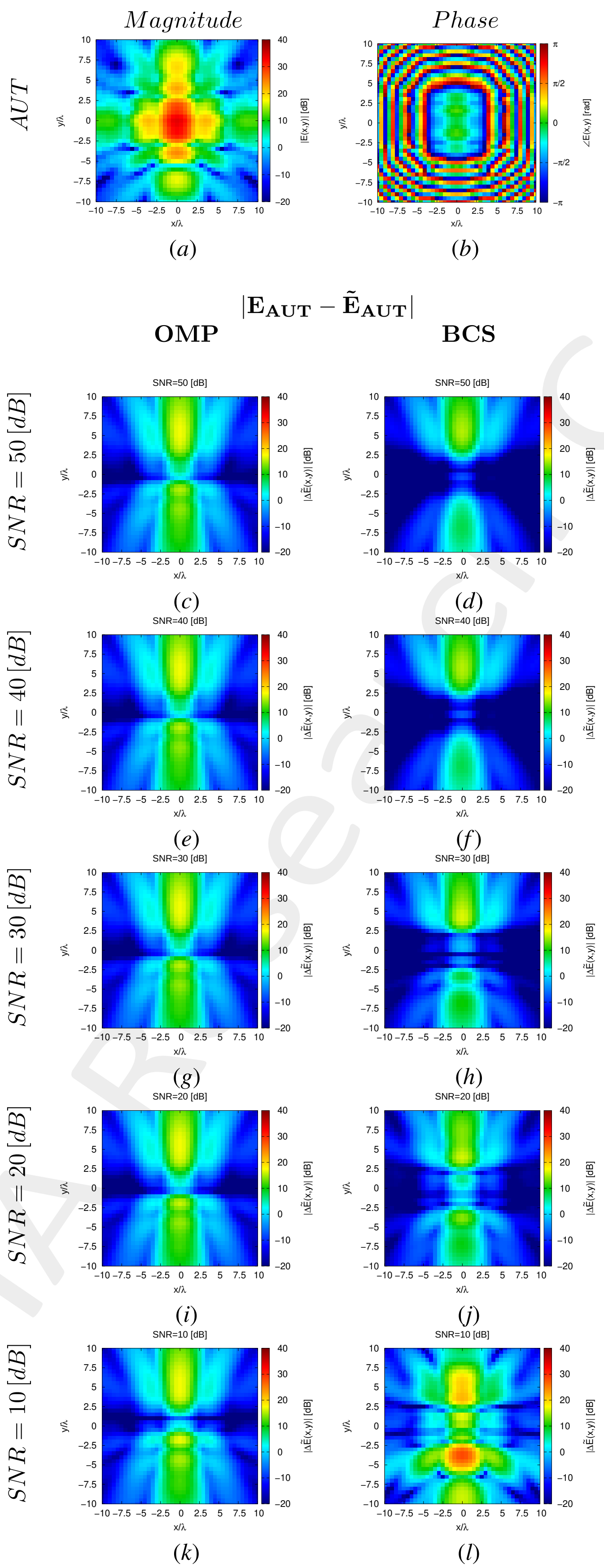

Figure 14: Magnitude difference between the actual and estimated $2-D$ near-field pattern when processing noisy measurements at different SNRs.

Estimated Far-Field

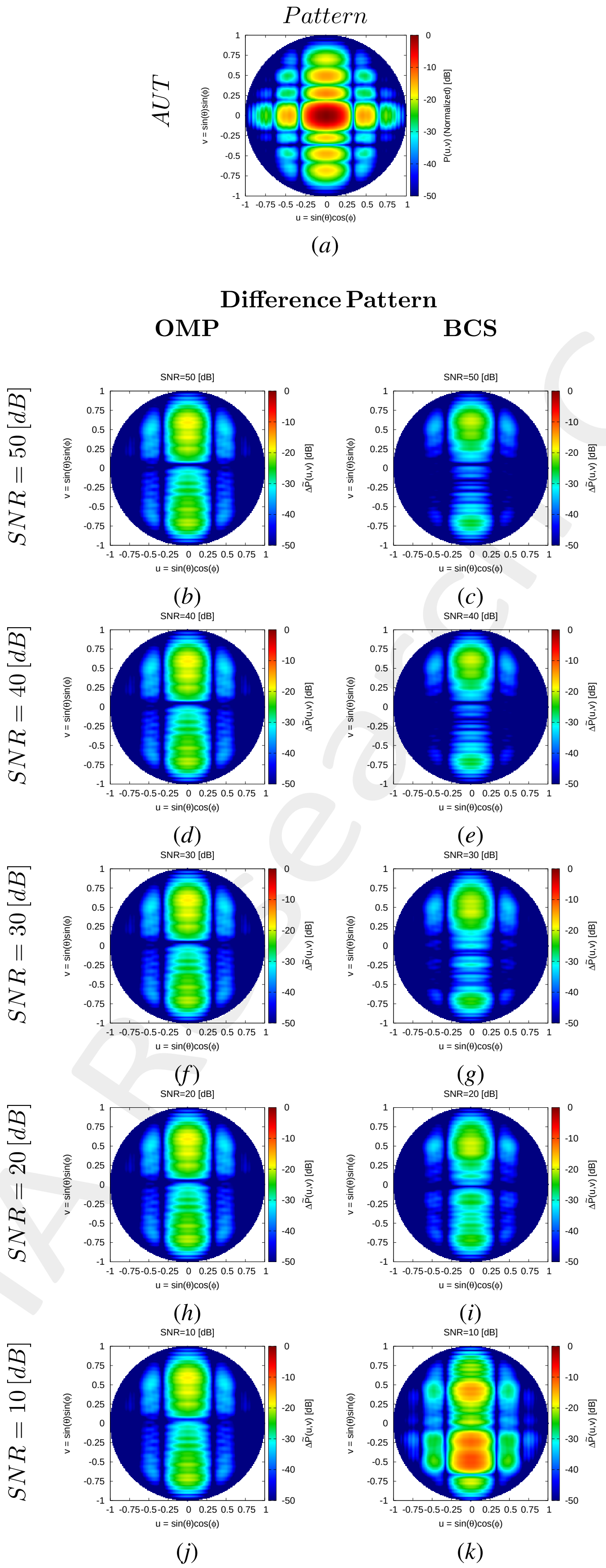

Figure 15: Difference between the actual and estimated $2-D$ far-field pattern when processing noisy measurements at different SNRs.

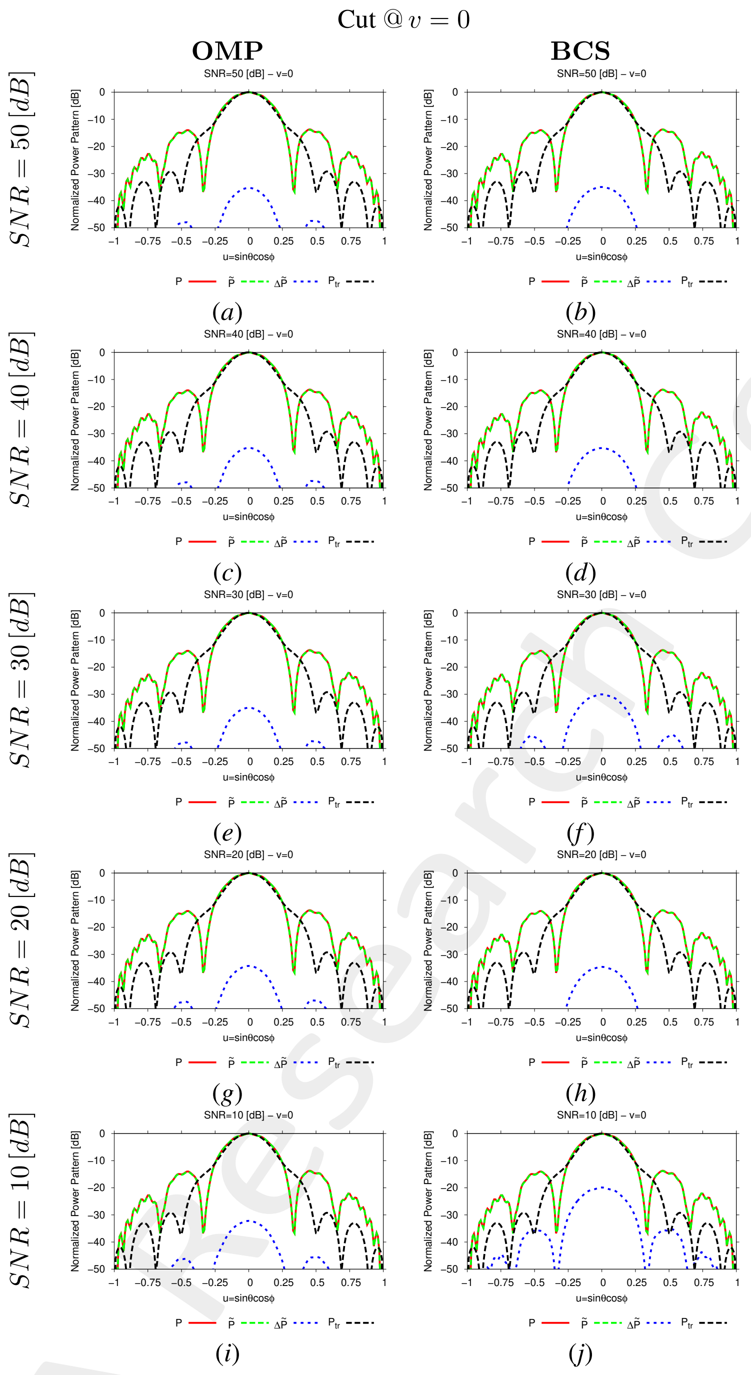

Figure 16: $1-D$ cuts of the estimated far-field pattern (obtained through near-to-far-field transformation from the estimated near-field patterns) under several noisy conditions

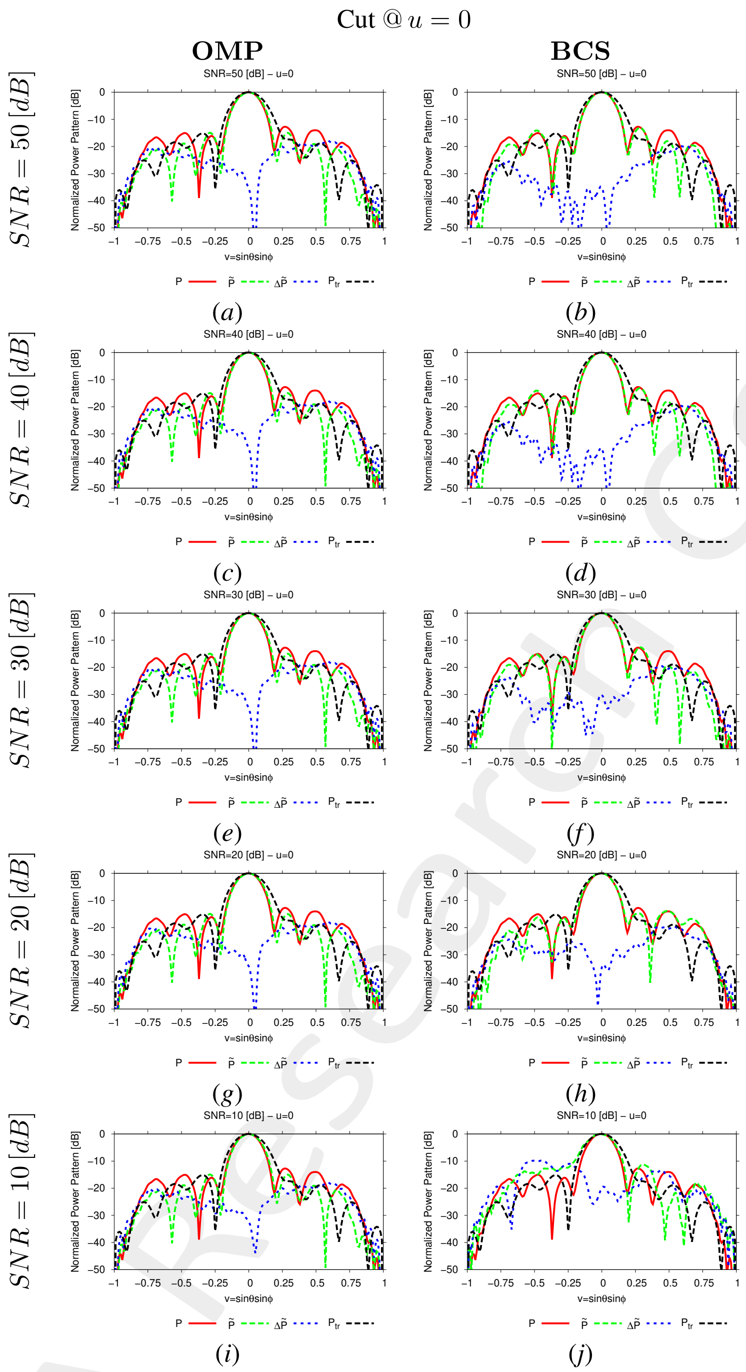

Figure 17: $1-D$ cuts of the estimated far-field pattern (obtained through near-to-far-field transformation from the estimated near-field patterns) under several noisy conditions

$SNR\,[dB]$	$Far-Field\ Error,\ \chi\ [dB]$	
	BCS	OMP
50	-17.28	-13.22
40	-17.23	-13.22
30	-16.18	-13.22
20	-15.80	-13.22
10	-6.01	-13.20

Table V: Far-field matching error between the actual and estimated AUT patterns (both obtained through near-to-far-field transformation from the corresponding near-field patterns) under several noisy conditions.

Estimated Coefficients

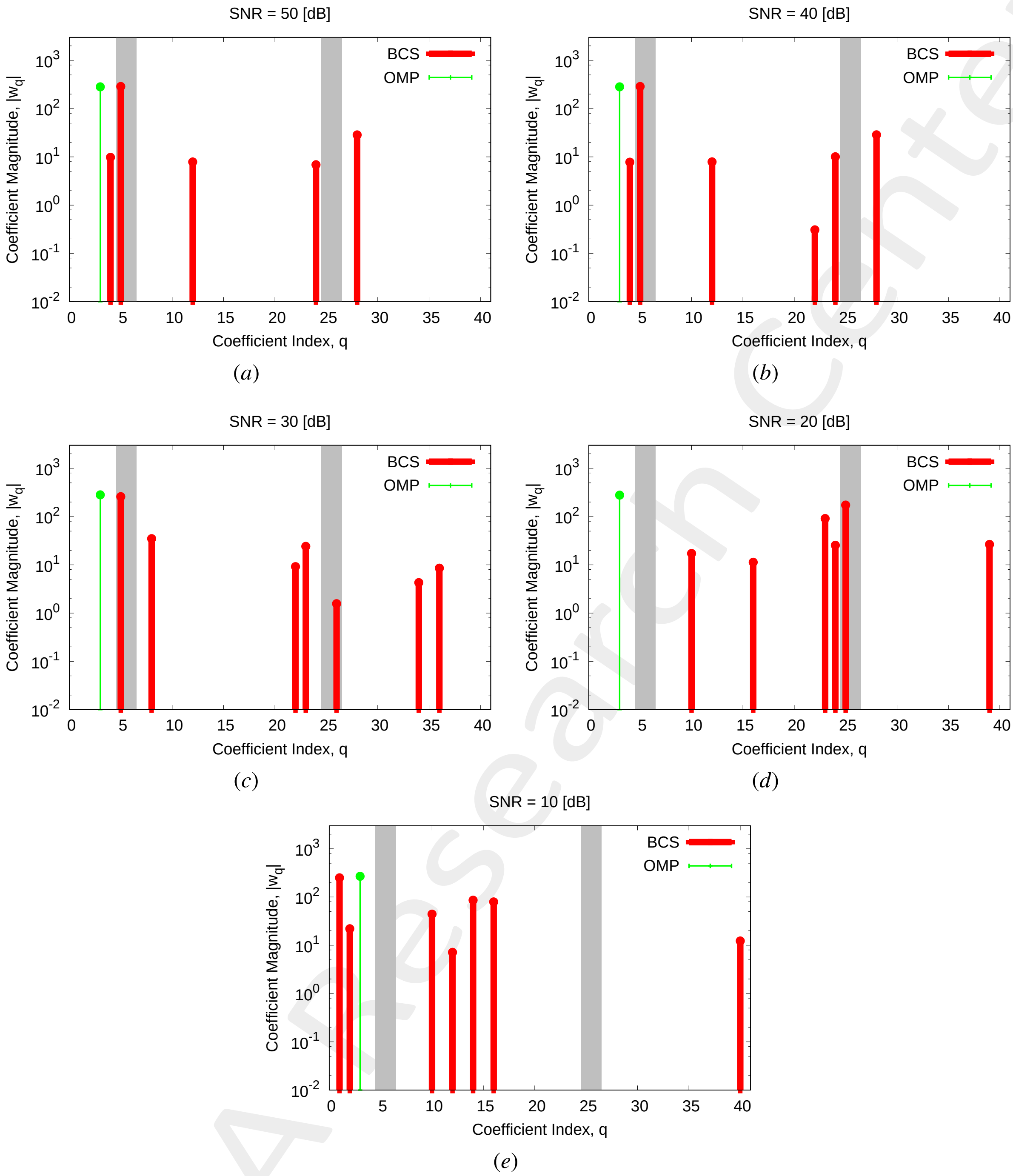

Figure 18: Coefficient comparison between original (*OMP*) and alternative (*BCS*) MbD : (*a*) $SNR = 50\,[dB]$, (*b*) $SNR = 40\,[dB]$, (*c*) $SNR = 30\,[dB]$, (*d*) $SNR = 20\,[dB]$, (*e*) $SNR = 10\,[dB]$

Observations

The considered *AUT* is characterized by a magnitude failure of an antenna element and a phase failure of another antenna element (i.e., $\nu^{(3)} = 0.45$ and $\gamma^{(3)} = \frac{\pi}{3}\,[rad]$):

- the *OMP* selects a single vector connected to a magnitude failure and it is not able to identify any failure actually affecting the *AUT*.
- the *BCS* algorithm, save at $SNR = 10\,[dB]$, is able to identify at least one failure affecting the AUT even if

the failure detections are not precise since the method selects also vectors not connected to the actual failures and it doesn't pick all the vectors of the failures affecting the *AUT*. In particular, the *BCS* identify both the failures affecting the *AUT* only at $SNR = 30\,[dB]$.

Computational times

- Δt_{Sim}: Time required to simulate the K *AUT* configurations used to build the $(T \times K)$ "pattern matrix";
- Δt_{SVD}: Time required to perform the *SVD* of the $(T \times K)$ "pattern matrix";
- $\Delta t_{MbE}^{OMP/BCS}$: (Mean) Time required by the Measurement-by-Example tool to read the *SVD* output and perform the estimation of the *AUT* radiated field.

Δt_{Sim} $[sec]$	4.17×10^4
Δt_{SVD} $[sec]$	1.53×10^2
Δt_{MbE}^{BCS} $[sec]$	1.72×10^{-1}
Δt_{MbE}^{OMP} $[sec]$	8.69×10^{-2}

Table VI: Computational times

Remarks

- Given that the number of simulated *AUT*s is $K = S \times (F^{(s)} + P^{(s)}) = 120$, the average per-*AUT* simulation time is

$$\Delta t_{FEKO} \simeq \frac{\Delta t_{Sim}}{K} = \frac{4.17 \times 10^4}{120} [sec] = 3.47 \times 10^2 \, [sec]$$

1.0.2 Overall Analysis

Near-Field Error Analysis

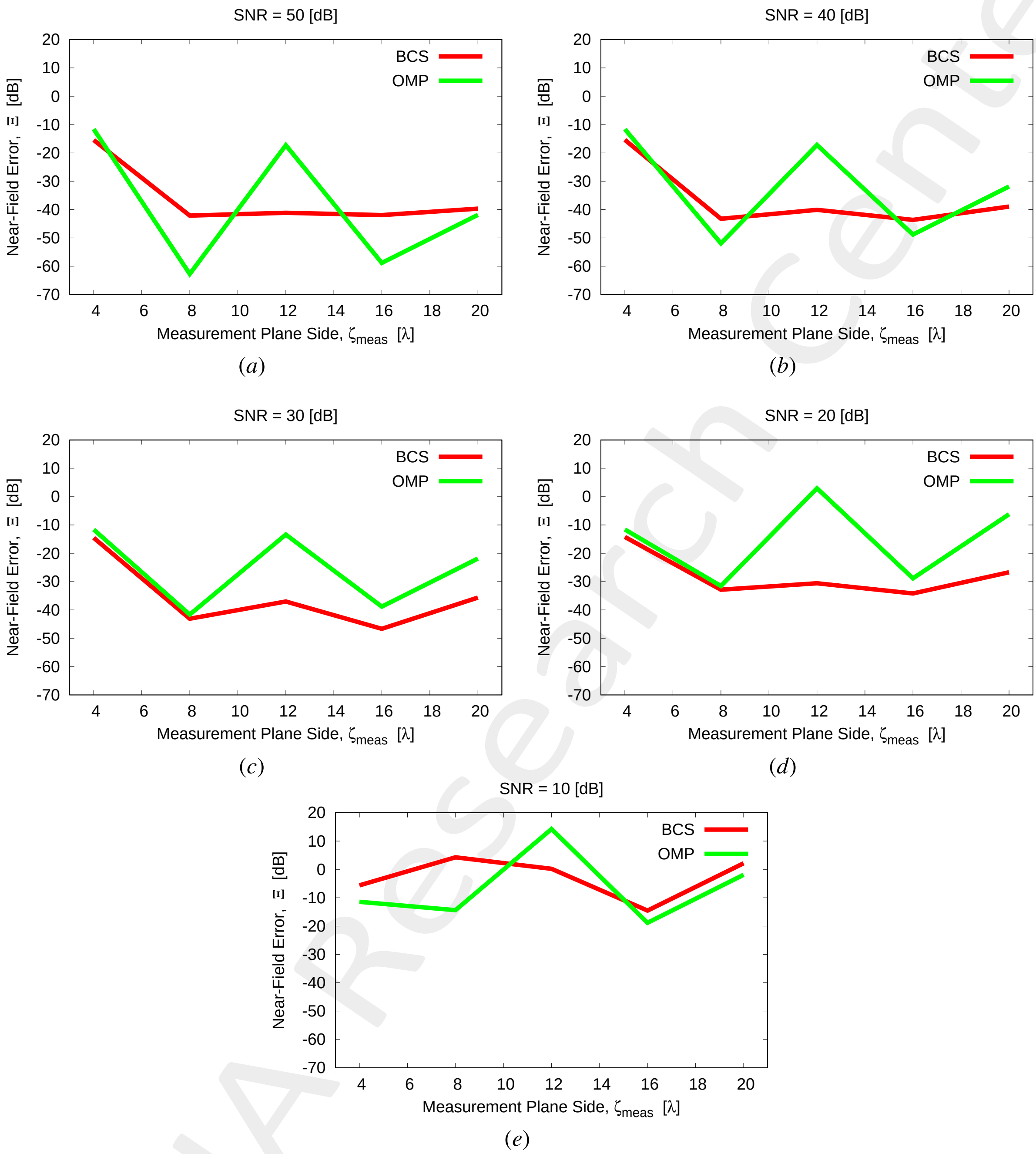

Figure 19: Near-field error vs measurement plane side (ζ_{meas}) dimension at different SNR values: (*a*) $SNR = 50\,[dB]$, (*b*) $SNR = 40\,[dB]$, (*c*) $SNR = 30\,[dB]$, (*d*) $SNR = 20\,[dB]$, (*e*) $SNR = 10\,[dB]$

Far-Field Error Analysis

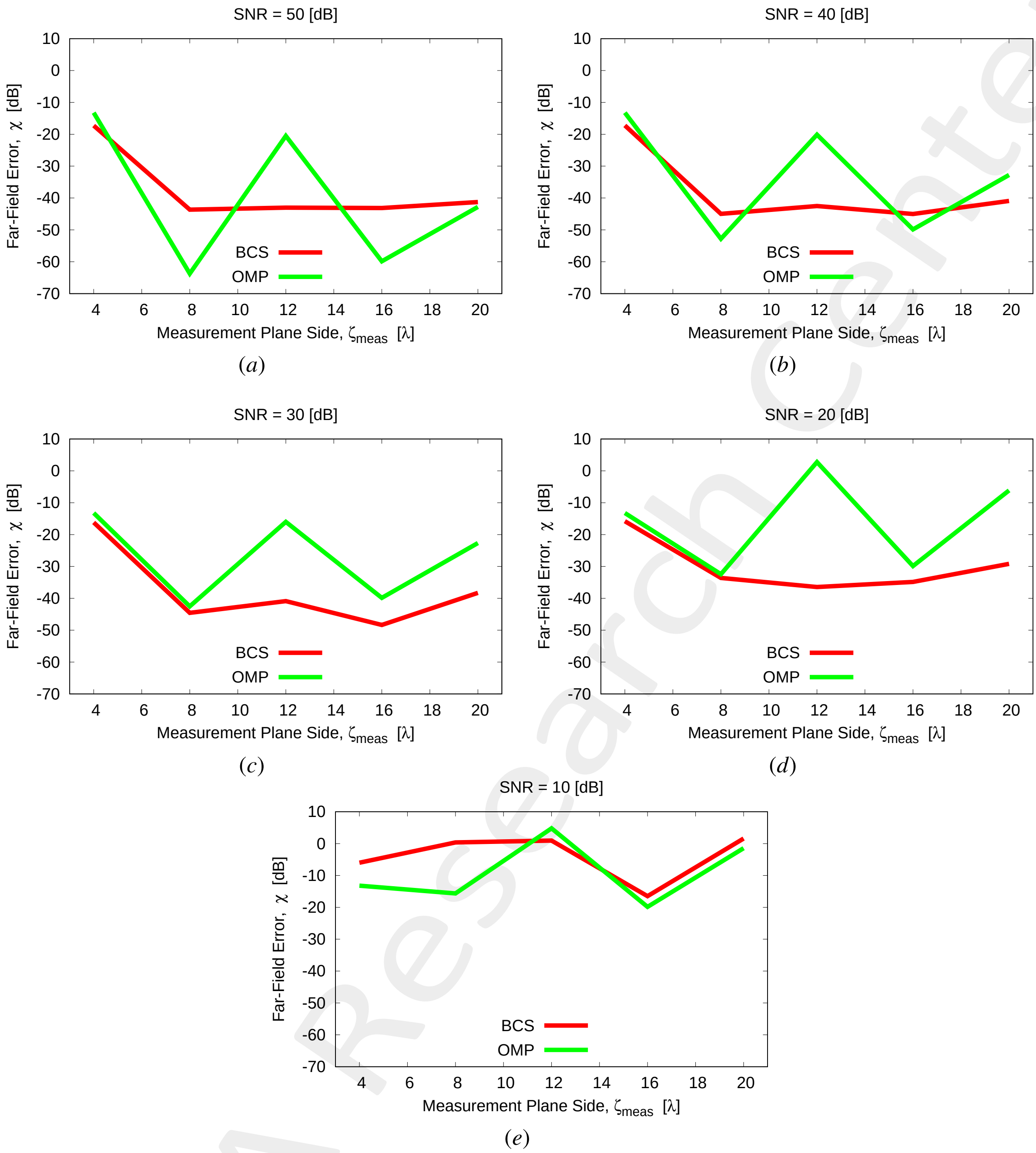

Figure 20: Far-field error vs measurement plane side (ζ_{meas}) dimension at different SNR values: *(a)* $SNR = 50\,[dB]$, *(b)* $SNR = 40\,[dB]$, *(c)* $SNR = 30\,[dB]$, *(d)* $SNR = 20\,[dB]$, *(e)* $SNR = 10\,[dB]$

Observations

From the reported results it is possible to point out that:

- the *OMP* algorithm performs better than the *BCS* at $SNR = 50,\ 40,\ 10\,[dB]$;
- the *BCS* solver outperforms the other one at $SNR = 20,\ 30\,[dB]$.

More information on the topics of this document can be found in the following list of references.

References

[1] M. Salucci, N. Anselmi, M. D. Migliore and A. Massa, “A bayesian compressive sensing approach to robust near-field antenna characterization,” *IEEE Trans. Antennas Propag.*, vol. 70, no. 9, pp. 8671-8676, Sep. 2022 (DOI: 10.1109/TAP.2022.3177528).

[2] B. Li, M. Salucci, W. Tang, and P. Rocca, “Reliable field strength prediction through an adaptive total-variation CS technique,” *IEEE Antennas Wirel. Propag. Lett.*, vol. 19, no. 9, pp. 1566-1570, Sep. 2020.

[3] M. Salucci, M. D. Migliore, P. Rocca, A. Polo, and A. Massa, “Reliable antenna measurements in a near-field cylindrical setup with a sparsity promoting approach,” *IEEE Trans. Antennas Propag.*, vol. 68, no. 5, pp. 4143-4148, May 2020.

[4] G. Oliveri, M. Salucci, N. Anselmi, and A. Massa, “Compressive sensing as applied to inverse problems for imaging: theory, applications, current trends, and open challenges,” *IEEE Antennas Propag. Mag. - Special Issue on "Electromagnetic Inverse Problems for Sensing and Imaging*,” vol. 59, no. 5, pp. 34-46, Oct. 2017.

[5] A. Massa, P. Rocca, and G. Oliveri, “Compressive sensing in electromagnetics - A review,” *IEEE Antennas Propag. Mag.*, pp. 224-238, vol. 57, no. 1, Feb. 2015.

[6] A. Massa and F. Texeira, “Guest-Editorial: Special Cluster on Compressive Sensing as Applied to Electromagnetics,” *IEEE Antennas Wirel. Propag. Lett.*, vol. 14, pp. 1022-1026, 2015.

[7] G. Oliveri, N. Anselmi, M. Salucci, L. Poli, and A. Massa, “Compressive sampling-based scattering data acquisition in microwave imaging,” *J. Electromagn. Waves Appl*, vol. 37, no. 5, 693-729, March 2023 (DOI: 10.1080/09205071.2023.2188263).

[8] G. Oliveri, L. Poli, N. Anselmi, M. Salucci, and A. Massa, “Compressive sensing-based Born iterative method for tomographic imaging,” *IEEE Trans. Microw. Theory Techn.*, vol. 67, no. 5, pp. 1753-1765, May 2019.

[9] M. Salucci, L. Poli, and G. Oliveri, “Full-vectorial 3D microwave imaging of sparse scatterers through a multi-task Bayesian compressive sensing approach,” *J. Imaging*, vol. 5, no. 1, pp. 1-24, Jan. 2019.

[10] M. Salucci, A. Gelmini, L. Poli, G. Oliveri, and A. Massa, “Progressive compressive sensing for exploiting frequency-diversity in GPR imaging,” *J. Electromagn. Waves Appl.*, vol. 32, no. 9, pp. 1164-1193, 2018.

[11] N. Anselmi, L. Poli, G. Oliveri, and A. Massa, “Iterative multi-resolution bayesian CS for microwave imaging,” *IEEE Trans. Antennas Propag.*, vol. 66, no. 7, pp. 3665-3677, Jul. 2018.

[12] N. Anselmi, G. Oliveri, M. A. Hannan, M. Salucci, and A. Massa, “Color compressive sensing imaging of arbitrary-shaped scatterers,” *IEEE Trans. Microw. Theory Techn.*, vol. 65, no. 6, pp. 1986-1999, Jun. 2017.

[13] N. Anselmi, G. Oliveri, M. Salucci, and A. Massa, "Wavelet-based compressive imaging of sparse targets" *IEEE Trans. Antennas Propag.*, vol. 63, no. 11, pp. 4889-4900, Nov. 2015.

[14] G. Oliveri, P.-P. Ding, and L. Poli, "3D crack detection in anisotropic layered media through a sparseness-regularized solver," *IEEE Antennas Wirel. Propag. Lett.*, vol. 14, pp. 1031-1034, 2015.

[15] L. Poli, G. Oliveri, P.-P. Ding, T. Moriyama, and A. Massa, "Multifrequency Bayesian compressive sensing methods for microwave imaging," *J. Opt. Soc. Am. A*, vol. 31, no. 11, pp. 2415-2428, 2014.

[16] G. Oliveri, N. Anselmi, and A. Massa, "Compressive sensing imaging of non-sparse 2D scatterers by a total-variation approach within the Born approximation," *IEEE Trans. Antennas Propag.*, vol. 62, no. 10, pp. 5157-5170, Oct. 2014.

[17] L. Poli, G. Oliveri, F. Viani, and A. Massa, "MT-BCS-based microwave imaging approach through minimum-norm current expansion," *IEEE Trans. Antennas Propag.*, vol. 61, no. 9, pp. 4722-4732, Sep. 2013.

[18] F. Viani, L. Poli, G. Oliveri, F. Robol, and A. Massa, "Sparse scatterers imaging through approximated multitask compressive sensing strategies," *Microwave Opt. Technol. Lett.*, vol. 55, no. 7, pp. 1553-1558, Jul. 2013.

[19] L. Poli, G. Oliveri, P. Rocca, and A. Massa, "Bayesian compressive sensing approaches for the reconstruction of two-dimensional sparse scatterers under TE illumination," *IEEE Trans. Geosci. Remote Sensing*, vol. 51, no. 5, pp. 2920-2936, May 2013.

[20] P. Rocca, N. Anselmi, M. A. Hannan, and A. Massa, "Conical frustum multi-beam phased arrays for air traffic control radars," *Sensors*, vol. 22, no. 19, 7309, pp. 1-18, 2022 (DOI: 10.3390/s22197309)

[21] F. Zardi, G. Oliveri, M. Salucci, and A. Massa, "Minimum-complexity failure correction in linear arrays via compressive processing," *IEEE Trans. Antennas Propag.*, vol. 69, no. 8, pp. 4504-4516, Aug. 2021.

[22] N. Anselmi, G. Gottardi, G. Oliveri, and A. Massa, "A total-variation sparseness-promoting method for the synthesis of contiguously clustered linear architectures," *IEEE Trans. Antennas Propag.*, vol. 67, no. 7, pp. 4589-4601, Jul. 2019.

[23] M. Salucci, A. Gelmini, G. Oliveri, and A. Massa, "Planar arrays diagnosis by means of an advanced Bayesian compressive processing," *IEEE Trans. Antennas Propag.*, vol. 66, no. 11, pp. 5892-5906, Nov. 2018.

[24] L. Poli, G. Oliveri, P. Rocca, M. Salucci, and A. Massa, "Long-Distance WPT Unconventional Arrays Synthesis," *J. Electromagn. Waves Appl.*, vol. 31, no. 14, pp. 1399-1420, Jul. 2017.

[25] G. Oliveri, M. Salucci, and A. Massa, "Synthesis of modular contiguously clustered linear arrays through a sparseness-regularized solver," *IEEE Trans. Antennas Propag.*, vol. 64, no. 10, pp. 4277-4287, Oct. 2016.

[26] M. Carlin, G. Oliveri, and A. Massa, "Hybrid BCS-deterministic approach for sparse concentric ring isophoric arrays," *IEEE Trans. Antennas Propag.*, vol. 63, no. 1, pp. 378-383, Jan. 2015.

[27] G. Oliveri, E. T. Bekele, F. Robol, and A. Massa, "Sparsening conformal arrays through a versatile BCS-based method," *IEEE Trans. Antennas Propag.*, vol. 62, no. 4, pp. 1681-1689, Apr. 2014.

[28] F. Viani, G. Oliveri, and A. Massa, “Compressive sensing pattern matching techniques for synthesizing planar sparse arrays,” *IEEE Trans. Antennas Propag.*, vol. 61, no. 9, pp. 4577-4587, Sept. 2013.

[29] P. Rocca, M. A. Hannan, M. Salucci, and A. Massa, “Single-snapshot DoA estimation in array antennas with mutual coupling through a multi-scaling BCS strategy,” *IEEE Trans. Antennas Propag.*, vol. 65, no. 6, pp. 3203-3213, Jun. 2017.

[30] M. Carlin, P. Rocca, G. Oliveri, F. Viani, and A. Massa, “Directions-of-arrival estimation through Bayesian Compressive Sensing strategies,” *IEEE Trans. Antennas Propag.*, vol. 61, no. 7, pp. 3828-3838, Jul. 2013.

[31] M. Carlin, P. Rocca, G. Oliveri, and A. Massa, “Bayesian compressive sensing as applied to directions-of-arrival estimation in planar arrays," *J. Electromagn. Waves Appl.*, vol.2013, pp.1-12, 2013 (DOI :10.1155/2013/245867).